Journal of Power Sources 377 (2018) 80–86

Contents lists available at ScienceDirect

Journal of Power Sources

journal homepage: www.elsevier.com/locate/jpowsour

Crystalline maricite $NaFePO_4$ as a positive electrode material for sodium secondary batteries operating at intermediate temperature

Jinkwang Hwang[a], Kazuhiko Matsumoto[a,d,*], Yuki Orikasa[b], Misaki Katayama[b], Yasuhiro Inada[b], Toshiyuki Nohira[c,d], Rika Hagiwara[a,d]

[a] Graduate School of Energy Science, Kyoto University, Yoshida-honmachi, Sakyo-ku, Kyoto 606-8501, Japan
[b] Department of Applied Chemistry, Ritsumeikan University, 1-1-1 Noji-higashi, Kusatsu Shiga 525-8577, Japan
[c] Institute of Advanced Energy, Kyoto University, Gokasho, Uji 611-0011, Japan
[d] Unit of Elements Strategy Initiative for Catalysts & Batteries (ESICB), Kyoto University, Katsura, Kyoto 615-8510, Japan

HIGHLIGHTS

- A maricite $NaFePO_4$ positive electrode is employed for sodium secondary batteries.
- Crystalline m-$NaFePO_4$ is electrochemically active at intermediate temperature.
- XRD reveals that m-$NaFePO_4$ undergoes desodiation-sodiation reaction.
- The interfacial resistance of m-$NaFePO_4$ is evaluated by EIS using symmetric cells.

GRAPHICAL ABSTRACT

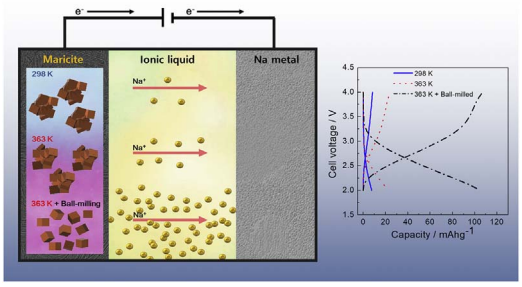

ARTICLE INFO

Keywords:
Sodium secondary batteries
Olivine
Maricite
Ionic liquid
Intermediate-temperature operation

ABSTRACT

Maricite $NaFePO_4$ (m-$NaFePO_4$) was investigated as a positive electrode material for intermediate-temperature operation of sodium secondary batteries using ionic liquid electrolytes. Powdered m-$NaFePO_4$ was prepared by a conventional solid-state method at 873 K and subsequently fabricated in two different conditions; one is ball-milled in acetone and the other is re-calcined at 873 K after the ball-milling. Electrochemical properties of the electrodes prepared with the as-synthesized m-$NaFePO_4$, the ball-milled m-$NaFePO_4$, and the re-calcined m-$NaFePO_4$ were investigated in Na[FSA]-[C_2C_1im][FSA] ($C_2C_1im^+$ = 1-ethyl-3-methylimidazolium, FSA^- = bis(fluorosulfonyl)amide) ionic liquid electrolytes at 298 K and 363 K to assess the effects of temperature and particle size on their electrochemical properties. A reversible charge-discharge capacity of 107 mAh g^{-1} was achieved with a coulombic efficiency > 98% from the 2nd cycle using the ball-milled m-$NaFePO_4$ electrode at a C–rate of 0.1 C and 363 K. Electrochemical impedance spectroscopy using m-$NaFePO_4$/m-$NaFePO_4$ symmetric cells indicated that inactive m-$NaFePO_4$ becomes an active material through ball-milling treatment and elevation of operating temperature. X-ray diffraction analysis of crystalline m-$NaFePO_4$ confirmed the lattice contraction and expansion upon charging and discharging, respectively. These results indicate that the desodiation-sodiation process in m-$NaFePO_4$ is reversible in the intermediate-temperature range.

* Corresponding author. Graduate School of Energy Science, Kyoto University, Yoshida-honmachi, Sakyo-ku, Kyoto 606-8501, Japan.
E-mail address: k-matsumoto@energy.kyoto-u.ac.jp (K. Matsumoto).

https://doi.org/10.1016/j.jpowsour.2017.12.003
Received 22 September 2017; Received in revised form 28 November 2017; Accepted 3 December 2017

1. Introduction

Lithium secondary batteries have been widely adopted as power sources for small devices owing to their high energy density [1–3]. However, this advantage of lithium secondary batteries is offset for large-scale energy storage applications by their high cost, including potential problems for constituent elements, and safety issues regarding the use of organic electrolytes. Thus, electrode materials free from trace elements have drawn attention as a means to strengthen the economic viability of sodium secondary batteries. Post-lithium secondary batteries have to be economically affordable and safe, and provide good electrochemical performance [4–8]. Owing to these factors, there is currently considerable interest in sodium secondary batteries for large-scale energy storage applications [9]. A number of reports have stated that the safety problems associated with lithium secondary batteries can be mitigated using ionic liquid (IL) electrolytes owing to their non-flammability, low volatility, and high thermal and electrochemical stabilities [10–13], and this is also true for sodium secondary batteries [14,15].

According to our previous studies, the elevation of operating temperature using IL electrolytes can enhance Na^+ diffusion both in the solid active material and the electrolyte, which effectively improves the electrochemical performances of positive and negative electrodes [16–21]. Thus, sodiation/desodiation into/from materials that are inactive at room temperature may be realized by elevating the operation temperature. Such elevated-temperature operation of secondary batteries is not impracticable for real applications. Indeed, it is even preferable in some cases considering the self-heating of batteries and their use in hot environments such as the engine compartments of automobiles.

Iron-based phosphates family such as Na_2FePO_4F, $Na_2FeP_2O_7$, and $Na_4Fe(PO_4)_2P_2O_7$ have been studied as potential positive electrode materials for sodium secondary batteries [22–27]. $NaFePO_4$, which is known to adopt an olivine structure with two polymorphs triphylite and maricite [28], has the highest theoretical capacity of 155 mAh g^{-1} among the iron-based phosphates. However, $NaFePO_4$ has not been deeply studied in detail owing to its difficult preparation (in the case of triphylite) or electrochemical inactivity (in the case of maricite). Triphylite $NaFePO_4$ (t-$NaFePO_4$) can be prepared by chemical and electrochemical Li-Na exchange process (i.e. delithiation of $LiFePO_4$ and sodiation of $FePO_4$, respectively) [28,29]. However, there are no reports of the direct synthesis of t-$NaFePO_4$ for a practical use, even though it delivers a reversible capacity of 120 mAh g^{-1} based on Fe^{3+}/Fe^{2+} redox activity [29]. Maricite $NaFePO_4$ (m-$NaFePO_4$) can be synthesized by conventional solid-state methods because it is thermodynamically stable phase [28]. However, m-$NaFePO_4$ was considered to be electrochemically inactive for a long time until a recent study by Kang's group [30], in which Na^+ was proved to be desodiated from nano-sized m-$NaFePO_4$ during the first charge, transforming the maricite phase into electrochemically active amorphous $FePO_4$. This phase exhibits a reversible capacity of 142 mAh g^{-1} at room temperature [30]. Although other research groups have also investigated the charge-discharge behavior of m-$NaFePO_4$ [31–33], no detailed reaction mechanism has been clarified and no improvements in performance for practical applications have sufficiently been achieved.

Our recent preliminary report demonstrated that m-$NaFePO_4$ exhibits a reversible capacity of 80 mAh g^{-1} at a C–rate of 0.2 C in a pyrrolidinium-based IL at 363 K [34]. Although it did not directly show the electrochemical activity of "crystalline" m-$NaFePO_4$, *ex-situ* XRD measurements suggested some crystalline m-$NaFePO_4$ is preserved, even after 100 cycles [34]. Since the reversible capacity achieved in this previous study was far from the theoretical value, further improvement was required.

In the present study, the ball-milling conditions have been reexamined in order to improve the performance of m-$NaFePO_4$ positive electrodes for intermediate-temperature sodium secondary batteries. Since ball-milling of m-$NaFePO_4$ with conductive carbon leads to irreversible capacity and degradation of battery performance, ball-milling was performed without adding conductive carbon [34]. Another improvement was the use of imidazolium-based IL electrolytes. Our previous study on $Na_2FeP_2O_7$ positive electrodes indicated that imidazolium-based ILs enable better rate performance by decreasing both bulk and interfacial impedances [20]. Here, m-$NaFePO_4$ electrodes prepared by three different conditions (as-synthesized, ball-milled, and re-calcined) were examined at 298 K and 363 K using the a Na[FSA]-[C_2C_1im][FSA] (C_2C_1im = 1-ethyl-3-methylimidazolium, FSA = bis (fluorosulfonyl)amide) IL electrolyte in order to clarify the activation mechanism of m-$NaFePO_4$. Furthermore, the effects of temperature and ball-milling conditions on the activation of m-$NaFePO_4$ were investigated by electrochemical impedance spectroscopy (EIS) using m-$NaFePO_4$/m-$NaFePO_4$ symmetric cells.

2. Experimental

2.1. Synthesis

A powdery sample of m-$NaFePO_4$ was synthesized by a conventional solid-state method [25]. Stoichiometric amounts of Na_2CO_3 (Wako Pure Chemical Industries, purity 99.8%), $FeC_2O_4{\cdot}2H_2O$ (Wako Pure Chemical Industries, purity 99%), and $(NH_4)_2HPO_4$ (Wako Pure Chemical Industries, purity > 99%) were ball-milled in acetone for 12 h at 600 rpm using a Fritsch Pulverisette 7 Premium Line. The mixture was collected and dried under vacuum for 24 h at 393 K and then thoroughly ground using a mortar and pestle. This precursor mixture was then calcined at 623 K for 3 h and heated at 873 K for 12 h under Ar flow, followed by cooling to room temperature. X-ray diffraction (XRD) patterns were measured using a Rigaku Smart Lab diffractometer with Cu-*K*α radiation (40 kV and 30 mA) to confirm the purity of the m-$NaFePO_4$. Rietveld refinement confirmed the absence of detectable impurities in the prepared m-$NaFePO_4$ in our previous report [34].

2.1.1. Fabrications of the synthesized m-$NaFePO_4$

Three types of m-$NaFePO_4$ were prepared: as-synthesized, ball-milled, and re-calcined. The ball-milling was performed using 1 mm diameter of zirconium oxide balls for 12 h at 600 rpm using a Fritsch Pulverisette 7 Premium Line in 20 mL of acetone to reduce the particle size of the m-$NaFePO_4$ (m-$NaFePO_4$: zirconium balls = 3: 1 in volume). The ball-milled (24 h) m-$NaFePO_4$ was prepared in the same condition except for the longer ball-milling time. The re-calcination was made by heating the ball-milled sample at 873 K for 12 h under Ar atmosphere. XRD patterns were measured again after the fabrications. The morphologies of the three types of m-$NaFePO_4$ were observed by field-emission scanning electron microscopy (FE-SEM, Hitachi SU-8020).

2.2. Electrochemical measurements

The electrochemical properties of the electrode materials were measured using 2032 coin-type cells at 298 K and 363 K. Sodium metal (Aldrich, purity 99.95%) cut into a disk (16 mm in diameter) and fixed on an Al plate current collector was used as the negative electrode. Positive electrodes were prepared using the three different m-$NaFePO_4$ samples described above. The working electrode sheet was prepared by mixing m-$NaFePO_4$, Super C65 as a conductive additive, and PTFE as a binder (75:20:5 wt%), and spreading the mixture with a pestle and mortar. The sheet was pressed onto an Al mesh to have a coating density of approximately 4 mg cm^{-2}. The salts Na[FSA] (Mitsubishi Materials Electronic Chemicals, purity > 99%) and [C_2C_1im][FSA] (Kanto Chemical, purity > 99.9%) were dried under vacuum for 24 h at 353 K. The Na[FSA]-[C_2C_1im][FSA] (3:7 M ratio) IL was used as the electrolyte [14]. A glass microfiber filter (Whatman GF/A) was impregnated with the electrolyte at 333 K under vacuum for 24 h prior to the assembly of the test cell.

Electrochemical properties were measured using a HJ1001SD8 charge-discharge test device (Hokuto Denko). All the measurements were conducted at least 3 h after temperature adjustment in an ESPEC thermostatic chamber. The symmetric cells for EIS were prepared using 2032 coin-type cells using three different m-$NaFePO_4$ samples. The cells were assembled as shown in Fig. S1 under a dry Ar atmosphere. The measurements were performed with a VSP potentiostat (Bio-Logic) at 298 K, 323 K, 343 K, and 363 K over a frequency range from 1 MHz to 1 mHz with a perturbation amplitude of 10 mV. In order to prepare samples for *ex-situ* XRD and X-ray absorption fine structure (XAFS) measurements, cells were disassembled in an Ar-filled glovebox and the electrodes were rinsed three times with dehydrated tetrahydrofuran (Wako Pure Chemical Industries, water content ≤ 10 ppm) in the glovebox and dried under vacuum at 333 K.

2.3. X-ray diffraction and absorption measurements

Ex-situ XRD measurements were performed using a Rigaku Smart Lab diffractometer. After electrochemical analysis, each dried electrode material was loaded into an airtight sample holder for measurement. XAFS measurement was performed using beam line BL-3 at the SR center, Ritsumeikan University. The electrode material was removed from the Al current collector, mixed with boron nitride powder, and pressed into a pellet for these measurements. Fe *K*-edge spectra were measured in transmission mode.

2.4. Particle size distributions and surface areas

Particle size distributions of the as-prepared m-$NaFePO_4$, the ball-milled (12 h) m-$NaFePO_4$, the ball-milled (24 h) m-$NaFePO_4$, and the re-calcined m-$NaFePO_4$ were measured using a Microtrac MT3300 II. N_2 gas adsorption measurement was carried out on a Micromeritics Tristar II. The samples were dried at 373 K under vacuum for 12 h before adsorption. The adsorption was performed at 77 K, and BET method was analyzed by Micromeritics software.

3. Results and discussion

Figs. 1 and 2 show the XRD patterns and SEM images of the as-synthesized, ball-milled, and re-calcined m-$NaFePO_4$ samples (see Fig. S2 for SEM images at different magnification). The XRD pattern of ball-milled m-$NaFePO_4$ for 12 h (Fig. 1b) confirms that it comprises pure maricite phase. However, some peak broadening compared to the pattern of the as-synthesized sample is observed (Fig. 1a) which is due to reduction of the crystallite size, as confirmed by the SEM images in Fig. 2b. The broad background may indicate that the ball-milled

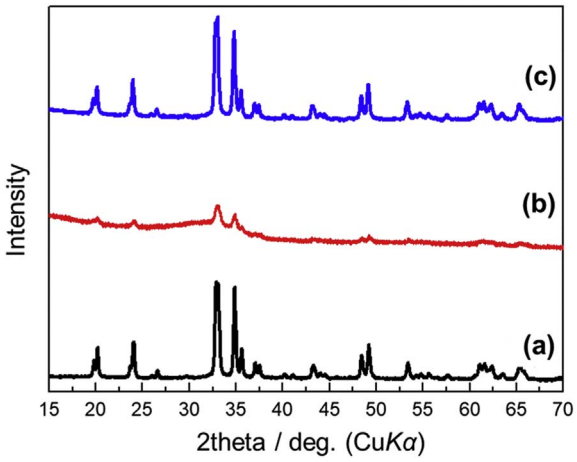

Fig. 1. X-ray diffraction patterns of (a) as-synthesized m-$NaFePO_4$, (b) ball-milled m-$NaFePO_4$, and (c) re-calcined m-$NaFePO_4$.

$NaFePO_4$ partly contains amorphous phase. However, longer ball-milling (24 h) did not result in complete amorphization (see Fig. S3, Supplementary Data).

The SEM image of the as-synthesized m-$NaFePO_4$ (Fig. 2a) indicates that the crystallite size ranges from 100 nm to 200 nm. The size is reduced to 50–100 nm upon ball-milling treatment (Fig. 2b). The XRD pattern of the re-calcined m-$NaFePO_4$ indicates a recovery of crystallinity to the same level as that of the as-prepared m-$NaFePO_4$ (Fig. 1c). After re-calcination, secondary particles grow more tightly than those in the original state (Fig. 2a and c), which is reflected in the poor charge-discharge performance of the re-calcined m-$NaFePO_4$, as discussed below. The precise particle size distribution of the samples was measured by the laser diffraction particle size analyzer (see Fig. S4 for particle size distribution). According to the results, the as-prepared m-$NaFePO_4$ mostly has the particle distribution range from 10 μm to 500 μm. After ball-milling treatment, the particle size distribution range shifted from 1 μm to 50 μm (longer ball-milling (24 h) shows similar result). After re-calcination, particle size distribution ranges from 100 μm to 1000 μm which is significantly larger than the size of the ball-milled $NaFePO_4$.

Fig. 3 shows the results of galvanostatic charge-discharge tests at a C-rate of C/10 (1C = 155 mA g^{-1}) under a cutoff voltage of 2.0 V–4.0 V. The as-synthesized m-$NaFePO_4$ electrode exhibits the very limited reversible capacity of 10 mAh g^{-1} at 298 K (Fig. 3a). This result is in agreement with previous recognition of that m-$NaFePO_4$ is an inactive positive electrode material at room temperature [28,29,31–34]. Although the reversible capacity of the as-synthesized m-$NaFePO_4$ is doubled upon elevating operating temperature to 363 K, the capacity is still only 20 mAh g^{-1} (Fig. 3b). Thus, although the elevation of operation temperature improves Na^+ diffusion in m-$NaFePO_4$, it is still very limited.

The ball-milled m-$NaFePO_4$ exhibits a reversible capacity of 23 mAh g^{-1} at 298 K (Fig. 3c) and 107 mAh g^{-1} at 363 K (Fig. 3d), demonstrating that the reversible capacity of m-$NaFePO_4$ is dramatically improved by the combination of the elevation of operating temperature ball-milling treatment. Although the coulombic efficiency for the initial cycle is 140.7% at 363 K, suggesting partial oxidation of the before charge electrode material (see XAFS analysis below), it reaches 98.1% for the second cycle. The ball-milling treatment in acetone efficiently reduces crystallite size, which shortens Na^+ diffusion paths in the solid state and increases surface area. Elevation of operating temperature also contributes to the improvement of Na^+ diffusion, both in the solid state and in the electrolyte. Prolonged ball-milling (24 h) does not significantly improve the reversible capacity of m-$NaFePO_4$ (104 mAh g^{-1} at 0.1 C and 113 mAh g^{-1} at 0.05 C, both at 363 K (Fig. S5, Supplementary Data). After re-calcination of the ball-milled m-$NaFePO_4$, the particles strongly aggregate each other, which makes the material inactive again and limits the reversible capacity to 6.9 mAh g^{-1} at 298 K and 14.2 mAh g^{-1} at 363 K (Fig. 3e and f). Surface area of the as-prepared, ball-milled, and re-calcined m-$NaFePO_4$ was measured by the N_2 gas adsorption method, since it can also affect the electrochemical activity. The resulting surface areas are 4.27, 7.15, and 3.24 m^2 g^{-1}, respectively (see Fig. S6 and S7 for details of surface area measurements). This result indicates that the surface area of the ball-milled m-$NaFePO_4$ is roughly twice larger than those of the as-prepared and re-calcined m-$NaFePO_4$, which does not contradict the SEM observation and suggests the increase of the electrochemically active sites in the ball-milled $NaFePO_4$. In our previous report [34], since ball-milling with conductive carbon resulted in unstable discharge behavior, the lower cutoff voltage had to be set above 2.2 V. On the other hand, ball-milling was performed without conductive carbon, enabling stable discharge down to 2.0 V in the present work. The conductive carbon ball-milled with active materials is thought to cause the reductive decomposition of ILs at 363 K.

The discharge rate and cycling performance of the ball-milled $NaFePO_4$ at 363 K are shown in Figs. 4 and 5, respectively. The

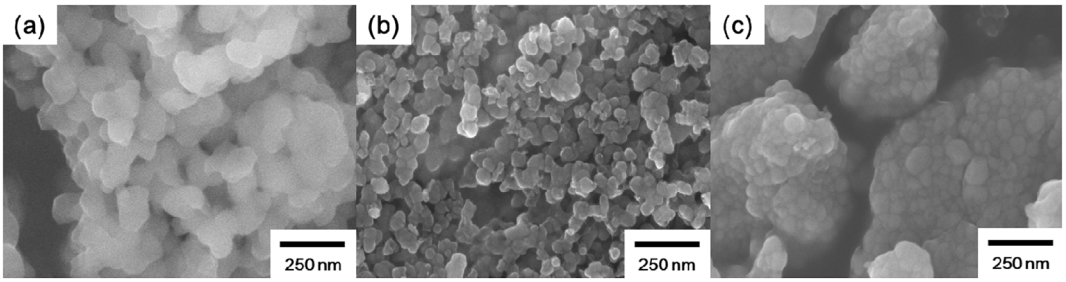

Fig. 2. FE-SEM images of (a) as-synthesized m-$NaFePO_4$, (b) ball-milled m-$NaFePO_4$, and (c) re-calcined m-$NaFePO_4$.

charging rate was 0.1 C for the first 5 cycles and was increased to 0.2 C for the rest of rate tests. The discharge current ranges from 0.1 C to 10 C. After the rate capability test, three cycles of charge-discharge were measured at 0.2 C to see recuperation of the cell.

The discharge capacity monotonously decreases with increasing current rate. Although the electrode reaction is constrained at high discharge rates because of the high activation energy for Na^+ diffusion, the discharge capacities are still 95.0 mAh g^{-1} at 0.5 C (10th cycle), 62.5 mAh g^{-1} at 1 C (15th cycle), and 40.0 mAh g^{-1} at 2 C (20th cycle). The capacity recuperation of the cell after rate capability test was about 87.4% in Fig. 4 (33rd cycle vs. 10th cycle). The cycling performance of the ball-milled m-$NaFePO_4$ was evaluated at 1 C with cutoff voltages of 2.0 V and 4.0 V. The cell is stabilized and the columbic efficiency reaches 99% by the 10th cycle, and the columbic

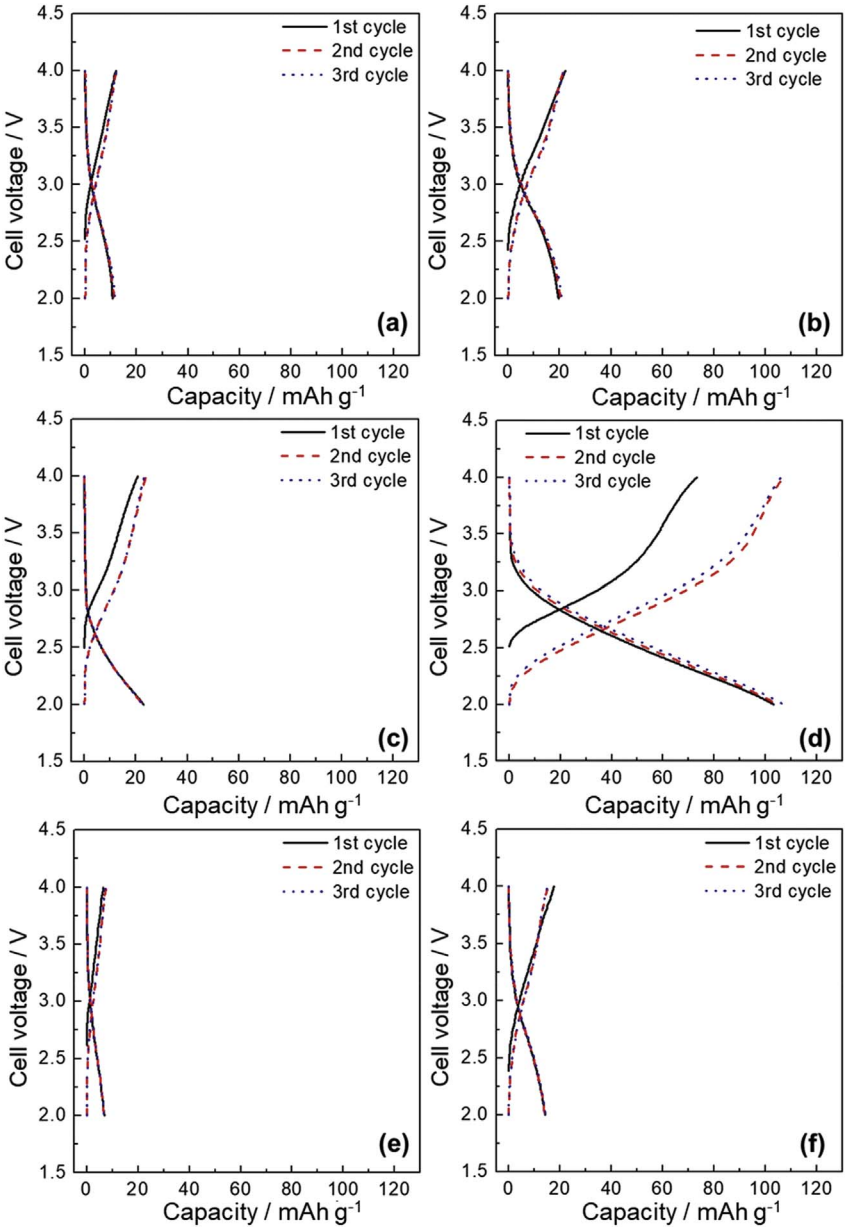

Fig. 3. Charge-discharge curves of Na/as-synthesized m-$NaFePO_4$ cells at (a) 298 K and (b) 363 K, Na/ball-milled m-$NaFePO_4$ cells at (c) 298 K and (d) 363 K, and Na/re-calcined m-$NaFePO_4$ cells at (e) 298 K and (f) 363 K. Electrolyte: Na[FSA]-[C_2C_1im][FSA], charge-discharge rate: C/10, and cutoff voltage: 2.0 V–4.0 V.

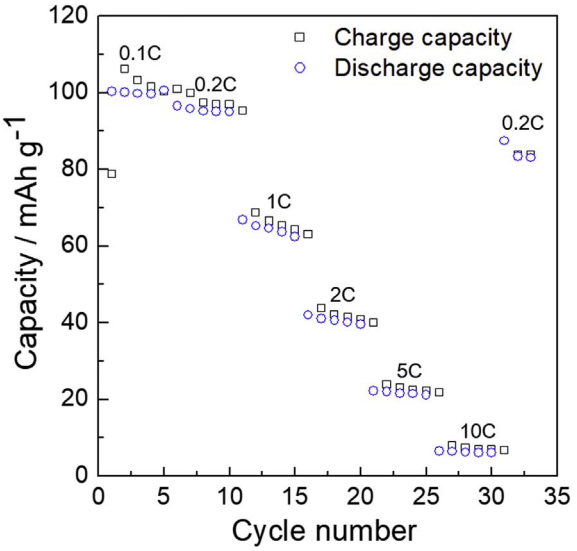

Fig. 4. Rate capability of a Na/ball-milled m-$NaFePO_4$ cell at 363 K. Cutoff voltage: 2.0 V–4.0 V.

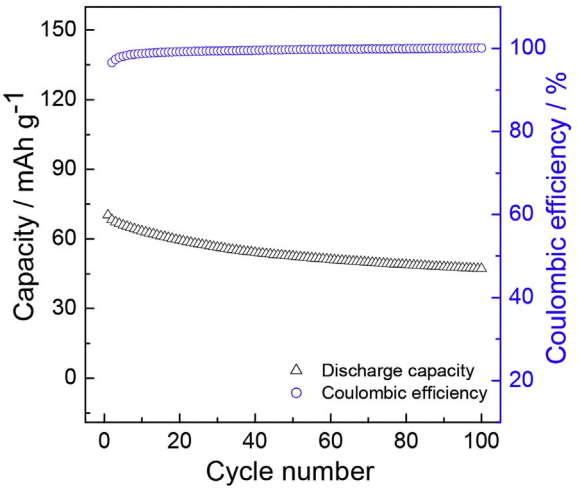

Fig. 5. Cyclability of a Na/ball-milled m-$NaFePO_4$ cell at 363 K. Black triangles indicate discharge capacity and blue circles indicate coulombic efficiency. Cutoff voltage: 2.0 V–4.0 V, C-rate: 1 C. (For interpretation of the references to colour in this figure legend, the reader is referred to the Web version of this article.)

efficiency exceeds 99.8% after the 50th cycle (Fig. 5). The capacity retention of the ball-milled m-$NaFePO_4$ is 67.2% after the 100th cycle.

To elucidate the reasons for the capacity enhancement by ball-milling and elevation of operating temperature, EIS was conducted at 298 K, 323 K, 343 K, and 363 K with symmetric cells using the as-synthesized, ball-milled, and re-calcined m-$NaFePO_4$. As shown in Fig. 6, each impedance plot is composed of two semicircles. The small semicircle at the higher frequency region (~10 kHz) is related to the resistance of the composite material (R_e) and is also observed in a control cell without active materials (i.e., prepared with acetylene black and PTFE only).

The other semicircle in the lower frequency region originates from the interfacial resistance on the electrode (R_{in}). The impedance spectra obtained were fitted by the equivalent circuit as shown in Fig. S8 (Supplementary Data). The same circuit was uniformly used for the three different fabricated samples at four different temperatures, and the Warburg impedance was not considered in the present cases since introduction of the Warburg impedance destabilizes the fitting especially for the re-calcined sample. According to the fitted parameters in Table S1 (Supplementary Data), the R_{in} value for the as-synthesized m-$NaFePO_4$ is considerably large at 298 K (15448 Ω), and the plot appears to be almost straight (Fig. 6a). With increasing temperature, the size of R_{in} decreases (1340 Ω), corresponding to the doubled capacity at 363 K from that at 298 K. The same trend is observed for the ball-milled and the re-calcined m-$NaFePO_4$ in Fig. 6b and c. Comparing the R_{in} values for the as-synthesized and ball-milled m-$NaFePO_4$ reveals that R_{in} dramatically decreases with ball-milling. After re-calcination, R_{in} increases again (Fig. 6c) to a value even higher than that of the as-synthesized m-$NaFePO_4$, which corresponds with the lower reversible capacity of the re-calcined m-$NaFePO_4$ than that of the as-synthesized sample (Fig. 3a, b, 3e, and 3f). These observations confirm that both the elevating temperature and ball-milling contribute to the reduction of R_{in} for the positive active material.

The *ex-situ* XRD data for the ball-milled m-$NaFePO_4$ indicate that the maricite phase is preserved, even after 50 cycles (Fig. S9, Supplementary Data). In addition, there seems to be some slight peak shifting to higher angles after charging followed by shifting back upon discharging (Fig. S9, Supplementary Data). However, the XRD peaks of the ball-milled m-$NaFePO_4$ are too weak and broad to ascertain whether the peak shifting originates from desodiation and sodiation of the maricite phase. Thus, the as-synthesized m-$NaFePO_4$, which exhibits higher crystallinity (Fig. 1a), was used to investigate the desodiation and sodiation mechanisms. Structural change was monitored by obtaining XRD patterns from the as-synthesized m-$NaFePO_4$ at different states of charge (SOCs). Four samples were prepared at 363 K for *ex-situ* XRD (Fig. S10, Supplementary Data).

After charge-discharge at a slow constant current rate (0.05 C), prolonged constant voltage charging was additionally applied until the cells exhibited a certain capacity. One of two cells was charged to 4.0 V at 0.05 C and maintained at 4.0 V for 10 h, reaching an SOC of 30%, and the other was charged to 4.0 V at 0.05 C and maintained at 4 V for 150 h reaching an SOC of 67%. The obtained XRD patterns are shown in Fig. 7. Slight peak shifting to higher angles is observed upon charging to SOC 30% and 67% (Fig. 7b and c), which indicates a

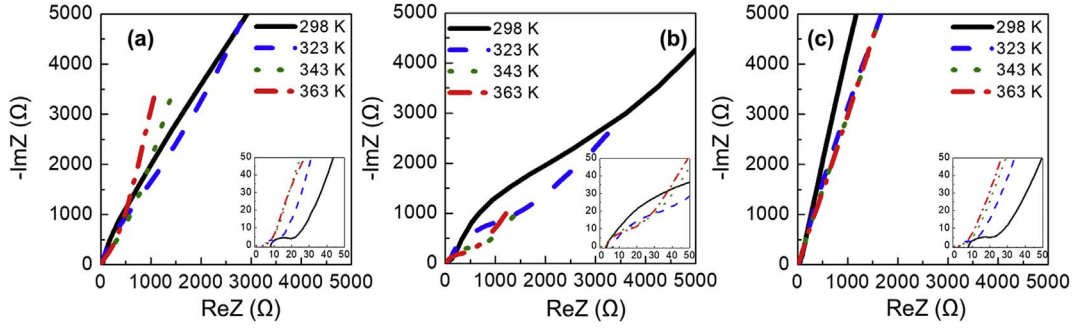

Fig. 6. Nyquist plots for (a) as-synthesized $NaFePO_4$/Na[FSA]-[C_2C_1im][FSA]/as-synthesized $NaFePO_4$, (b) ball-milled $NaFePO_4$/Na[FSA]-[C_2C_1im][FSA]/ball-milled $NaFePO_4$, and (c) re-calcined $NaFePO_4$/Na[FSA]-[C_2C_1im][FSA]/re-calcined $NaFePO_4$ symmetric cells in the temperature range between 298 K and 363 K. AC perturbation: 10 mV, frequency range: 1 MHz–10 mHz.

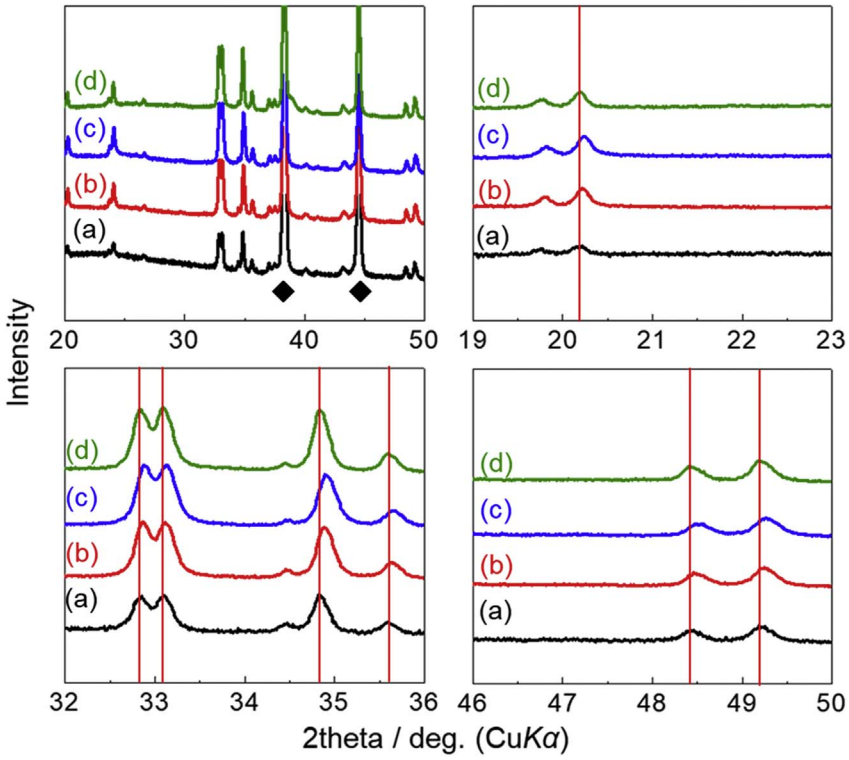

Fig. 7. *Ex-situ* XRD patterns of the as-synthesized m-$NaFePO_4$ electrode (a) before charge-discharge testing, (b) charged to 4 V at 0.05 C and maintained at constant current, constant voltage (CCCV) for 10 h, (c) charged to 4 V at 0.05 C and maintained at CCCV for 150 h, and (d) charged to 4 V at 0.05 C, maintained at CCCV for 150 h, discharged to 2 V at 0.05 C, and maintained at CCCV for 150 h. All electrochemical measurements were performed at 363 K. The ♦ symbols indicate the peaks for Al. The red perpendicular lines are reference lines to clarify XRD peak shifting. The charge-discharge profile used to prepare *ex-situ* XRD samples are shown in Fig. S10. (For interpretation of the references to colour in this figure legend, the reader is referred to the Web version of this article.)

decrease in d-spacing owing to desodiation. The peaks return to their original positions upon discharging at 0.05 C to 2.0 V followed by constant voltage discharging at 2.0 V for 150 h (Fig. 7d), indicating that sodiation of the maricite phase proceeds at 363 K. Fig. S11 shows the *ex-situ* XRD pattern of the as-synthesized m-$NaFePO_4$ at 298 K, and no peak shifting is observed. This result further demonstrates that m-$NaFePO_4$ is an inactive material at room temperature, which is consistent with the lack of sodiation-desodiation demonstrated in Fig. 4a. However, elevating the temperature changes m-$NaFePO_4$ into an active material, and ball-milling can further improve its electrochemical performance.

The X-ray absorption near edge structure (XANES) spectra of the ball-milled m-$NaFePO_4$ (before charge, charged, and discharged) are shown in Fig. 8. The main edge at 7120 eV shifts to the higher energy upon charging, which is explained by the oxidation of iron to Fe^{3+} during desodiation. Conversely, the main edge of the sample discharged to 2.0 V is shifted to lower energy, which indicates the reduction of Fe^{3+} to Fe^{2+} by sodiation. However, the main edge for the discharged sample is located at a lower energy than that of the before charge sample. The energy difference between the samples before charge and after the first cycle is thought to originate from partial oxidation of Fe^{2+} to Fe^{3+} in the sample before charge during the prolonged ball-milling treatment since reduction of iron to the lower oxidation state than +2 leads to the unstable conversion reaction. This is also reflected in the small charge capacity in the first cycle, as shown in Fig. 3d. In order to prove that air atmosphere oxidizes the electrodes, XANES of the ball-milled m-$NaFePO_4$ samples that were kept in the air for two weeks were measured. After the exposure to the air, the main edges of the ball-milled m-$NaFePO_4$ before charge and after first cycle were located at the same position which was higher than that of the sample before charge (Fig. S12, Supplementary Data).

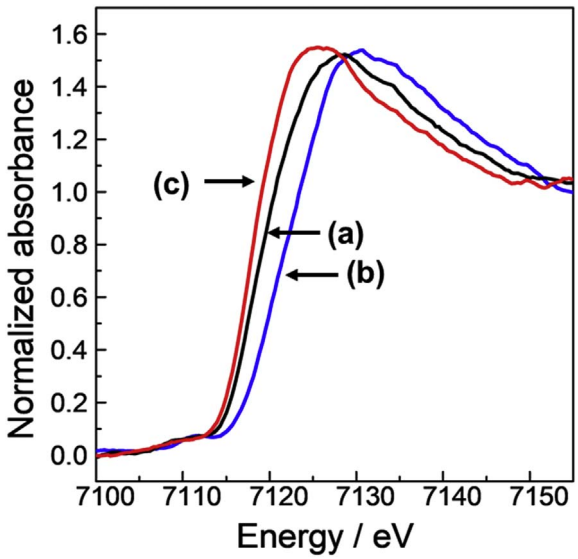

Fig. 8. Fe *K*-edge XANES spectra of ball-milled $NaFePO_4$ electrodes: (a) before charge, (b) charged to 4.0 V, and (c) discharged to 2.0 V.

4. Conclusion

We have investigated the electrochemical properties of m-$NaFePO_4$ as a positive electrode material for sodium secondary batteries using Na[FSA]-[C_2C_1im][FSA] IL electrolytes. The charge-discharge profiles show that the reversible capacity of m-$NaFePO_4$ is increased by ball-milling and elevation of the cell operation temperature. The ball-milled m-$NaFePO_4$ delivers a reversible capacity of 107 mAh g^{-1} at C/10 at 363 K. The reason for the capacity increase was elucidated by the results of EIS using symmetric cells. The interfacial impedance is significantly reduced with elevating temperature and with decreasing crystallite size. Finally, peak shifting in the *ex-situ* XRD patterns has been confirmed for the first time, indicating that sodiation and desodiation proceed in the maricite phase at elevated temperature. Thus, the elevation of operation temperature using ILs, not only improves the performance of an electrode, it can transform an inactive electrode material into a promising active electrode material for intermediate-temperature operating sodium secondary batteries.

Acknowledgments

This study was partly supported by the Advanced Low Carbon Technology Research and Development Program (ALCA) of the Japan Science and Technology Agency (JST) and the Japanese Ministry of Education, Culture, Sports, Science and Technology (MEXT) program “Elements Strategy Initiative to Form Core Research Center (ESICB)”.

Appendix A. Supplementary data

Supplementary data related to this article can be found at http://dx.doi.org/10.1016/j.jpowsour.2017.12.003.

References

[1] B. Dunn, H. Kamath, J.M. Tarascon, Science 334 (2011) 928.
[2] J.-M. Tarascon, M. Armand, Nature 414 (2001) 359.
[3] M.R. Palacin, Chem. Soc. Rev. 38 (2009) 2565.
[4] J.-M. Tarascon, Nat. Chem. 26 (2010) 510.
[5] P.W. Gruber, P.A. Medina, G.A. Keoleian, S.E. Kesler, M.P. Everson, T.J. Wallington, J. Ind. Ecol. 15 (2011) 760.
[6] A.K. Padhi, J. Electrochem. Soc. 144 (1997) 1188.
[7] L. Fang, J. Xiao, X. Qian, H. Ai, Y. Yang, Cao, Nano Lett. 14 (2014) 3539.
[8] J.W. Choi, D. Aurbach, Nat. Rev. Mater. 1 (2016) 16013.
[9] M.D. Slater, Adv. Funct. Mater. 23 (2013) 947.
[10] H. Matsumoto, H. Sakaebe, K. Tatsumi, M. Kikuta, E. Ishiko, M. Kono, J. Power Sources 160 (2006) 1308.
[11] S. Seki, Y. Kobayashi, H. Miyashiro, Y. Ohno, A. Usami, Y. Mita, N. Kihira, M. Watanabe, N. Terada, J. Phys. Chem. B 110 (2006) 10228.
[12] J.H. Shin, W.A. Henderson, S. Passerini, J. Electrochem. Soc. 152 (2005) A978.
[13] B. Garcia, S. Lavallée, G. Perron, C. Michot, M. Armand, Electrochim. Acta 49 (2004) 4583.
[14] K. Matsumoto, T. Hosokawa, T. Nohira, R. Hagiwara, A. Fukunaga, K. Numata, E. Itani, S. Sakai, K. Nitta, S. Inazawa, J. Power Sources 265 (2014) 36.
[15] K. Matsumoto, Y. Okamoto, T. Nohira, R. Hagiwara, J. Phys. Chem. C 119 (2015) 7648.
[16] C. Ding, T. Nohira, R. Hagiwara, K. Matsumoto, Y. Okamoto, A. Fukunaga, S. Sakai, K. Nitta, S. Inazawa, J. Power Sources 269 (2014) 124.
[17] C.-Y. Chen, K. Matsumoto, T. Nohira, R. Hagiwara, J. Electrochem. Soc. 162 (2014) A176.
[18] C.-Y. Chen, K. Matsumoto, T. Nohira, C. Ding, T. Yamamoto, R. Hagiwara, Electrochim. Acta 133 (2014) 583.
[19] T. Yamamoto, T. Nohira, R. Hagiwara, A. Fukunaga, S. Sakai, K. Nitta, Electrochim. Acta 211 (2016) 234.
[20] C.-Y. Chen, T. Kiko, T. Hosokawa, K. Matsumoto, T. Nohira, R. Hagiwara, J. Power Sources 332 (2016) 51.
[21] C.-Y. Chen, K. Matsumoto, T. Nohira, R. Hagiwara, J. Electrochem. Soc. 162 (2015) A2093.
[22] C.-Y. Chen, K. Matsumoto, T. Nohira, R. Hagiwara, Y. Orikasa, Y. Uchimoto, J. Power Sources 246 (2014) 783.
[23] Y. Zhu, Y. Xu, Y. Liu, C. Luo, C. Wang, Nanoscale 5 (2013) 780.
[24] P. Barpanda, T. Ye, S.-J. Chung, Y. Yamada, M. Okubo, H. Zhou, A. Yamada, Electrochem. Commun. 24 (2012) 116.
[25] P. Barpanda, G. Liu, C.D. Ling, M. Tamaru, M. Avdeev, S.-C. Chungm, Y. Yamada, A. Yamada, Chem. Mater. 25 (2013) 3480.
[26] H. Kim, R.A. Shakoor, C. Park, S.Y. Kim, J.-S. Kim, Y.N. Jo, W. Cho, K. Miyasaka, R. Kahraman, Y. Jung, J.W. Choi, Adv. Func. Mater. 23 (2013) 1147.
[27] A. Yamada, MRS Bull. 39 (2014) 423.
[28] M. Avdeev, Z. Mohamed, C.D. Ling, J. Lu, M. Tamaru, A. Yamada, P. Barpanda, Inorg. Chem. 52 (2013) 8685.
[29] S. Oh, S.-T. Myung, J. Hassoun, B. Scrosati, Y.-K. Sun, Electrochem. Commun. 22 (2012) 149.
[30] J. Kim, D. Seo, H. Kim, I. Park, J. Yoo, S. Jung, Y. Park, W.A. Goddard III, K. Kang, Energy Environ. Sci. 8 (2015) 540.
[31] P. Paolo Prosini, C. Cento, A. Masci, M. Carewska, Solid State Ion. 263 (2014) 1.
[32] M.M. Rahman, I. Sultana, S. Mateti, J. Liu, N. Sharma, Y. Chen, J. Mat. Chem. A 5 (2017) 16616.
[33] R. Kapaev, A. Chekannikov, S. Novikova, S. Yaroslavtsev, T. Kulova, V. Rusakov, A. Skundin, A. Yaroslavtsev, J. Solid State Electrochem. 21 (2017) 2373.
[34] J. Hwang, K. Matsumoto, T. Nohira, R. Hagiwara, Electrochemistry 85 (2017) 675.